# Coupled nuclear-electronic decay dynamics of $O_2$ inner valence excited states revealed by attosecond XUV wave-mixing spectroscopy

Yen-Cheng Lin[1,2], Ashley P. Fidler[1,2], Arvinder Sandhu[3], Robert R. Lucchese[1], C. William McCurdy[1,4], Stephen R. Leone[1,2,5], Daniel M. Neumark[1,2,*]

[1] Chemical Sciences Division, Lawrence Berkeley National Laboratory, Berkeley, California 94720, USA

[2] Department of Chemistry, University of California, Berkeley, California 94720, USA

[3] Department of Physics, University of Arizona, Tucson, Arizona 85721, USA

[4] Department of Chemistry, University of California, Davis, California 95616, USA

[5] Department of Physics, University of California, Berkeley, CA 94720, USA

[*] dneumark@berkeley.edu

## Abstract

Multiple Rydberg series converging to the $O_2^+$ $c\ ^4\Sigma_u^-$ state, accessed by 20-25 eV extreme ultraviolet (XUV) light, serve as important model systems for the competition between nuclear dissociation and electronic autoionization. The dynamics of the lowest member of these series, the $3s\sigma_g$ state around 21 eV, has been challenging to study owing to its ultra-short lifetime (< 10 fs). Here, we apply transient wave-mixing spectroscopy with an attosecond XUV pulse to investigate the decay dynamics of this electronic state. Lifetimes of 5.8±0.5 fs and 4.5±0.7 fs at 95% confidence intervals are obtained for v=0 and v=1 vibrational levels of the *3s* Rydberg state, respectively. A theoretical treatment of predissociation and electronic autoionization finds that these lifetimes are dominated by electronic autoionization. The strong dependence of the electronic autoionization rate on the internuclear distance because of two ionic decay channels that cross the *3s* Rydberg state results in the different lifetimes of the two vibrational levels. The calculated lifetimes are highly sensitive to the location of the *3s* potential with respect to the decay channels; by slight adjustment of the location, values of 6.2 and 5.0 fs are obtained computationally for the v=0 and v=1 levels, respectively, in good agreement with experiment. Overall, an intriguing picture of the coupled nuclear-electronic dynamics is revealed by attosecond XUV wave-mixing spectroscopy, indicating that the decay dynamics are not a simple competition between isolated autoionization and predissociation processes.

# I. Introduction

The competition between autoionization and predissociation in highly excited molecular electronic states is of great interest to the scientific community[1-7] as it addresses the coupling between electronic and nuclear degrees of freedom in a fundamental way. Studies on such systems provide insights into the potential energy surfaces of these states, along with the electron correlation and non-adiabatic effects that drive their decay dynamics. Until recently, these dynamics have been inferred from frequency-domain measurements, such as linewidths in absorption cross sections from synchrotron or electron scattering experiments.[5, 8-12] However, the advent of ultrafast light sources in the XUV region of the spectrum has enabled direct measurements of excited state lifetimes through novel spectroscopic techniques, thereby opening new windows into the decay mechanisms of these states.[13-16] In this paper, we employ the recently developed method of attosecond XUV wave-mixing spectroscopy[17-23] to very short-lived (<10 fs) Rydberg states of $O_2$ and, in conjunction with state-of-the-art theory, unravel the interplay between autoionization and predissociation with vibrational state-specificity.

The Rydberg series converging to the $O_2^+$ $c\ ^4\Sigma_u^-$ state represent a good model to study such competing decay dynamics and have thus been extensively investigated during the past few decades.[8-16, 24-39] The interaction of $O_2$ with 20-25 eV extreme ultraviolet (XUV) photons excites an inner shell $2\sigma_u$ electron to the Rydberg states comprising these series. There are two such series observed in the XUV absorption spectrum, denoted as $2\sigma_u^{-1}nl\sigma_g(l = 0,2)$, here abbreviated as *ns* and *nd* Rydberg series.[15, 24] As shown in Figure 1(a), these Rydberg states lie above several ionic states. They can thus undergo electronic autoionization through the rearrangement of their electronic structure, in which electron correlation couples states with different molecular orbital occupancies. Moreover, as shown in Figure 1(b), the Rydberg and ionic states have shallow wells that support a small number of vibrational levels and can undergo predissociation via tunneling.

Direct lifetime measurements can give insight into competing pathways, when linewidth measurements are not easy to deconvolve due to spectral congestion and overlap. For two competing parallel pathways, the observed decay rate (inverse lifetime) is the sum of the decay rates of each channel as shown in Equation (1)

$$\frac{1}{\tau^{(nl,\mathrm{v})}} = \frac{1}{\tau_a^{(nl,\mathrm{v})}} + \frac{1}{\tau_d^{(nl,\mathrm{v})}} \tag{1}$$

where *nl* specifies the electronic quantum numbers of the Rydberg electron, v is the vibrational quantum number of the *nl* state, and $\tau^{(nl,\mathrm{v})}$, $\tau_a^{(nl,\mathrm{v})}$, and $\tau_d^{(nl,\mathrm{v})}$ are the overall, autoionization, and predissociation lifetimes, respectively. This equation (when multiplied by $\hbar$) is simply the assertion that the partial widths of a metastable

state in scattering or photoionization add up to the total width, which is usually true to a good approximation.[40]

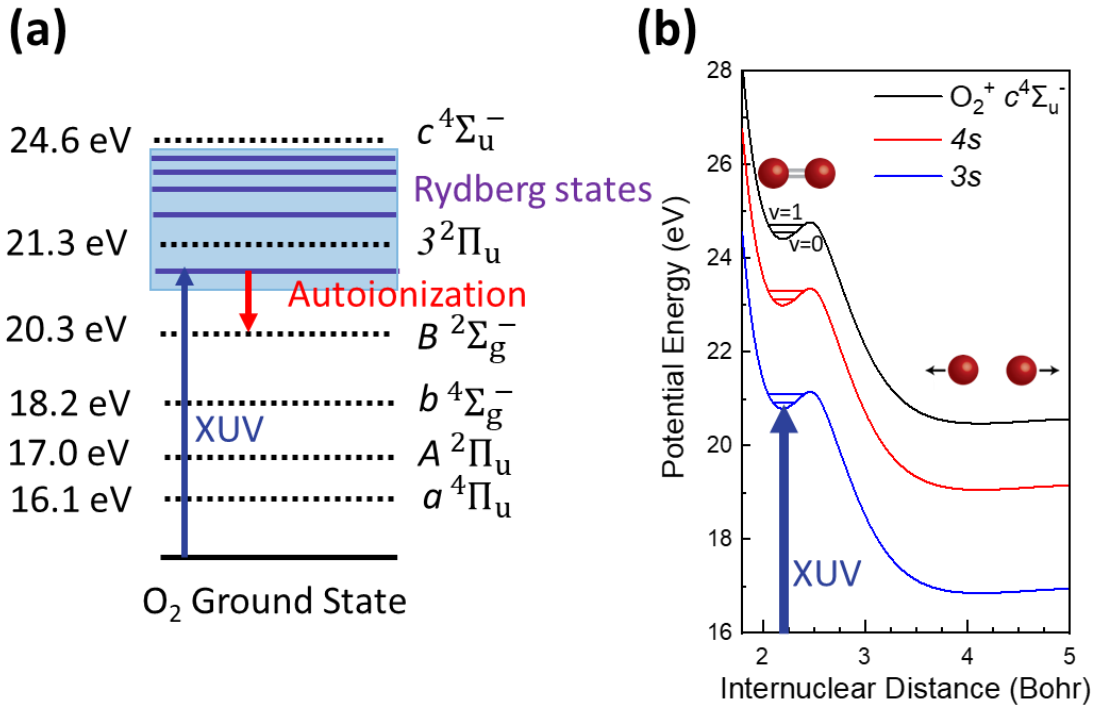


Figure 1. (a) Energy level diagram of $O_2^+$ states and Rydberg states converging to $O_2^+$ $c\,^4\Sigma_u^-$ state. The values of ionization potentials are from Ref [31]. The Rydberg states are energetically above several ionic states, to which they can autoionize. (b) Schematic potential energy curves of $O_2^+$ $c\,^4\Sigma_u^-$ state and its *3s* and *4s* Rydberg states

In the ion-core approximation, an electron in a Rydberg orbital is a spectator to nuclear motion, and the potential energy curves of the Rydberg states are approximately parallel to the ionic state to which they converge as shown in Figure 1(b).[5, 9-11, 15, 34-36, 38, 41] Therefore, both the vibrational structure and predissociation dynamics of Rydberg states are similar to those of the corresponding ionic state. The predissociation lifetimes are then largely independent of the principal quantum number of the Rydberg state, while depending strongly on the vibrational level. On the other hand, electronic autoionization is known to vary significantly within a Rydberg series, but its rate has generally been assumed to be independent of vibrational quantum number for this system.[11, 14, 37] With these assumptions, Eq. 1 could be approximated as

$$\frac{1}{\tau^{(nl,v)}} \approx \frac{1}{\tau_a^{(nl)}} + \frac{1}{\tau_d^{(v)}} \qquad (2)$$

Eq. (2) has been invoked frequently to explain the lifetime behavior of the

Rydberg series converging to the $O_2^+$ $c\ ^4\Sigma_u^-$ state.[11, 13-16, 36, 37] Three different vibrational levels of the $O_2^+$ $c\ ^4\Sigma_u^-$ state have been observed by photoelectron spectroscopy, namely v=0, v=1, and v=2.[31] The v=2 level is slightly above the barrier of the predissociation potential. The relative Franck-Condon factors are 1: 042: 0.015 for v=0, v=1 and v=2, respectively,[31] and the v=2 level has yet to be observed in the neutral Rydberg series. The predissociation lifetime ($\tau_d$) has been measured and calculated to be ~11 ps[5, 14, 37] and ~ 65 fs[9-11, 13, 38] for the v=0 and v=1 levels, respectively, in the $O_2^+$ $c\ ^4\Sigma_u^-$ state, and predissociation is thought to be similar and dominant in the decay of higher *n* Rydberg states.[5, 9, 11] Autoionization, on the other hand, becomes a competing and even dominant channel for the lower *n* Rydberg states. For example, autoionization lifetimes ($\tau_a$) of ~90 fs and ~180 fs were measured for *4d*/*5s* and *5d*/*6s* Rydberg states with pump-probe photoionization spectroscopy.[14, 16]

Eq. (2) implies that nuclear and electronic motion are independent. i.e., vibrational excitation does not change the electronic autoionization lifetime. Thus, lifetime differences among vibrational levels in the same electronic state were previously attributed to differing predissociation rates.[11, 36] However, recent studies of core-excited states suggest that the rate of Auger decay in diatomic molecule can be strongly bond-distance dependent and thus different vibrational states can give different Auger decay lifetimes.[42-44] Such phenomena should be observed in electronic autoionization if there is a strong coupling between electronic and nuclear motion. The lowest member in the Rydberg series, namely the *3s* Rydberg state, is a good candidate for this investigation as several ionic potentials cross near its equilibrium geometry.[16] However, in contrast to the higher *n* Rydberg states, which have been studied extensively[13-16], there are no previous direct time-domain measurements of the lifetime of the *3s* Rydberg state due to its ultra-short lifetime. Frequency domain measurements coupled with theory suggest linewidths of 145 meV and 154 meV for the v=0 and v=1 levels of the *3s* Rydberg state,[11, 37] respectively, corresponding to lower bounds on the lifetimes of 4.5 fs and 4.3 fs, respectively.

Recent advances in pulse compression techniques and high harmonic generation (HHG)[45-47] allow one to generate few-femtosecond near-infrared (NIR) pulses and attosecond XUV pulses at well-controlled time delays. This development has enabled several different kinds of pump-probe experiments, such as attosecond transient absorption (ATA), which have been used to investigate dynamics ranging from tens of femtoseconds to sub-fs. While ATA is now used in many laboratories[15, 44, 48-55], the resulting spectra are often complicated by spectral effects produced when pulses overlap such as the AC stark effect[49] and strong-field line shape control.[50] These effects are interesting in their own right but make it difficult to extract lifetime

information when the pulse duration is similar to the lifetime of interest. To disentangle this complexity, we recently developed attosecond non-collinear wave-mixing spectroscopy with one attosecond XUV pulse and two non-collinear few-femtosecond NIR pulses[17-23]. The advantage of the technique is that it spatially isolates the nonlinear response from the combined linear and nonlinear response of ATA and yields a background-free homodyne measurement that can be more cleanly interpreted than ATA. It has been used to probe the electronic and vibrational structure in atoms and molecules[17-19], and we utilized it recently to measure autoionization lifetimes in Kr.[21]

In this work, we report the first application of attosecond XUV wave-mixing spectroscopy to the fast-decaying dynamics in a molecule, specifically the $O_2$ *3s* Rydberg state. Spatially isolated wave-mixing signals are observed from this Rydberg state and the transient behavior of these signals is measured. The few-femtosecond resolution of the technique allows for direct lifetime measurements in the *3s* Rydberg state. The lifetimes for the v=0 and v=1 vibrational levels of the *3s* Rydberg state are obtained to be 5.8±0.5 fs and 4.5±0.7 fs, respectively. To explore the basis for the difference in these lifetimes, we perform *ab initio* electron-ion scattering calculations at multiple fixed internuclear distances and use the results in numerical calculations of the coupled nuclear and electronic dynamics. This theoretical description allows the details of vibrational motion to determine the effects of the varying electronic autoionization probability at each internuclear distance. The results from both experimental and theoretical work provide significant insights into the decay dynamics of the $O_2$ *3s* Rydberg state, indicating a subtle interplay between electronic autoionization rate and nuclear dynamics that drives the observed lifetimes.

# II. Method

## A. Experimental Setup

The experimental apparatus for attosecond non-collinear wave-mixing spectroscopy with attosecond XUV pulses has been described previously[21-23] and is shown in Figure 2. Briefly, a commercial Ti-sapphire laser system (Femtopower HE, Femtolasers) is used to produce 2 mJ, 22 fs NIR pulses at a 1 kHz repetition rate, which are then spectrally broadened in a 2 m long stretched hollow core fiber of 500 μ inner diameter filled with 2 bar of neon gas. Seven pairs of double-angle chirped mirrors (PC70, Ultrafast Innovations) followed by a 2 mm thick ammonium dihydrogen phosphate (ADP) crystal are used to temporally compress the pulses.[56] The resulting 5 fs broadband pulses are centered at 760 nm (~1.63 eV) with 600 μJ/ pulse. These pulses then impinge on a 25:75 beam splitter. The majority of the pulse is transmitted and focused into a vacuum apparatus ($10^{-6}$ Torr) by a concave silver

mirror (f = 50 cm). It passes through a 1 mm path length gas cell with flowing xenon gas at approximately 5 Torr for high harmonic generation to produce attosecond pulses in the XUV region. The co-propagating NIR pulses are filtered out by a 0.15 μ thick Al foil. The transmitted XUV pulses are refocused by a gold-coated toroidal mirror (f = 50 cm) into a 1 mm path length target gas cell filled with $O_2$ (10 Torr backing pressure) passing through pinholes drilled for the entrance and exit of the wave mixing beams.

The reflected pulse from the 25:75 beam splitter is delayed relative to the XUV pulse using a piezoelectric stage (P-622 with E509 controller, Physik Instrumente (PI)) and further split into two separate arms with a 50:50 beam splitter. The two separate beams are each focused by concave silver mirrors (f = 1 m) and directed to reflect vertically above and below the hole of an annular mirror. Eventually, these two beams cross the XUV pulses in the target gas cell at angles of approximately 18 mrad (1.0º) and 13 mrad (0.75º) for the lower (NIR 1) and upper arms (NIR 2), respectively, to generate wave-mixing signals at different angles as shown in Figure 2(b). The angles of the two beams are purposely set to be different based on phase matching considerations, as will be discussed in Sec. III B. The combined NIR intensity is about $10^{13}$ W/cm$^2$ in this experiment. Temporal and spatial overlap between the XUV and both NIR arms is determined by transient absorption signal with helium gas. A 0.15 μ thick Al foil is placed after the target gas cell to filter out the two NIR pulses. The transmitted XUV pulse and wave-mixing signal are dispersed by a gold-coated flat field concave grating (001-0639, Hitachi) and recorded by a 1340 × 400 pixel X-ray CCD camera (Pixis XO 400B, Princeton Instruments); the long horizontal axis represents the frequency of light dispersed by the grating and the vertical axis measures the emission angle of the light.

In the transient wave-mixing experiment, the two NIR pulses are set to be time-coincident at the overlap region, and we only change the relative delay between the XUV pulse and two coincident NIR pulses with the piezoelectric stage as shown in Figure 2(c). Positive delays indicate that the XUV pulse arrives at the sample earlier than the NIR pulses and vice versa for negative delays. To measure the lifetimes of the $O_2$ *3s* Rydberg states, delays between -10 fs to 50 fs are scanned with 1 fs steps. At each delay time, signals are accumulated for 30,000 laser pulses.

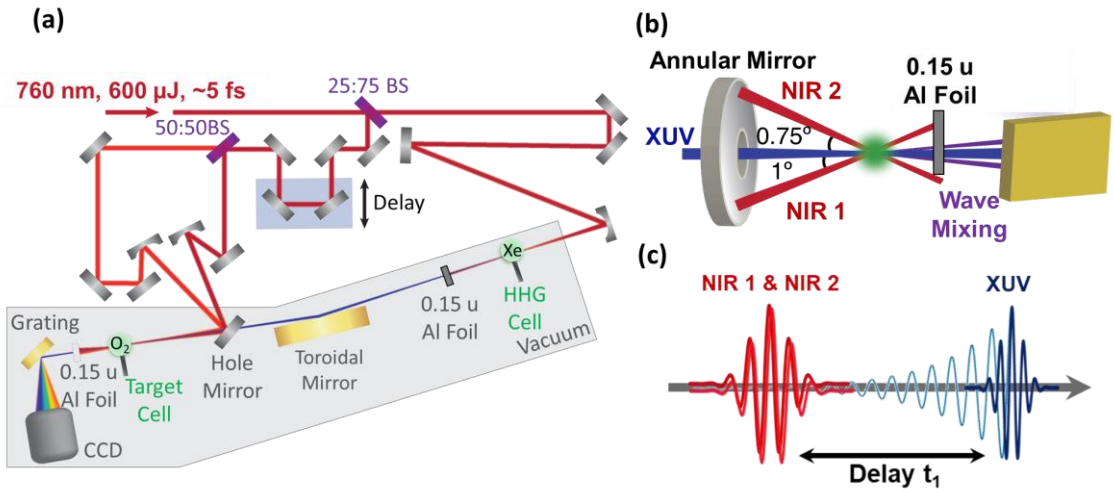


Figure 2. (a) Schematic of the experimental apparatus after NIR pulse compression (b) Interaction region of the three pulses. The NIR beams at angles of 1° and 0.75° with respect to the XUV beam are labeled NIR 1 and NIR 2, respectively. (c) Pulse sequence used to collect transient wave-mixing signals. Two time-coincident NIR pulses are delayed relative to the XUV pulse. The faint blue signal depicts the decay of the $O_2$ polarization that is probed by the NIR pulses through wave mixing.

## B. Theoretical Methods

In the first step to describe the effect of vibrational motion on electronic autoionization of the $O_2$ *3s* Rydberg state, photoionization calculations are performed very similar to those reported previously[16] over a range of internuclear distances. We employed the multichannel Schwinger variational method[57, 58] which is described further in several earlier applications to a variety of systems including $O_2$ .[59-61]

In these calculations, the final-state fixed-energy photoelectron wave functions are represented on a single center expanded grid that can be extended far enough to describe a number of Rydberg states below each ionization threshold. The full *N*-electron ionized state is represented as a close-coupling expansion containing a sum of the products of (*N* - 1)-electron ion state wave functions times one-electron photoelectron wave functions. The ion channels used in the close coupling calculation included $X\ ^2\Pi_g$, $a\ ^4\Pi_u$, $A\ ^2\Pi_u$, $b\ ^4\Sigma_g^-$, $B\ ^2\Sigma_g^-$,$1\ ^4\Pi_g$, $3\ ^2\Pi_u$, and $c\ ^4\Sigma_u^-$ states. At each internuclear distance R, a set of orbitals was computed with an aug-cc-pVTZ basis[62, 63] using MOLPRO[64, 65] with a complete-active-space-self-consistent field (CASSCF) description of the ground state keeping the $1\sigma_g$ and $1\sigma_u$ core orbitals doubly occupied. The various *N* - 1 electron ion states were then obtained from a complete active space configuration interaction calculation using the orbitals from the ground state CASSCF calculation.

These photoionization calculations produced detailed cross sections with

autoionization features corresponding to members of the various Rydberg series converging to the thresholds for producing differing ion states, like those in previous studies using these methods[16, 61]. Those cross sections vary strongly with internuclear distance, as the various nearby thresholds, and their associated Rydberg series, pass through the energy of the *3s* Rydberg state studied here, as indicated in Figure 3.

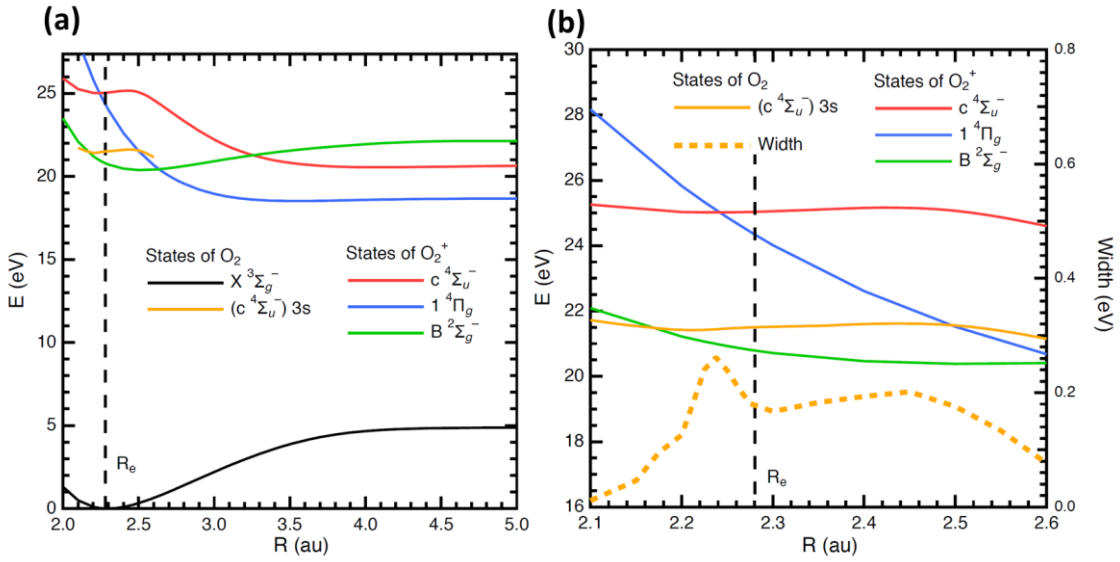


Figure 3. (a) Ground state potential curve of $O_2$ and some potential curves of the $O_2^+$ ion from MRCI calculations, plotted together with the real part of the energy of the *3s* Rydberg autoionizing state from the multichannel Schwinger calculations. (b) Magnification of the range of R over which the scattering calculations were performed also showing width of the *3s* Rydberg state and the thresholds for ionization leading to the $1\ ^4\Pi_g$ and $B\ ^2\Sigma_g^-$ states of $O_2^+$ that cross it.

The *3s* Rydberg state was fit with a Fano profile at eighteen different internuclear distances between 2.1 and 2.6 Bohr, which is the range of vibrational motion in the well and the barrier that binds the v=0 and v=1 vibrational levels of the *3s* Rydberg state. These fits produce both the width and the position of the autoionizing *3s* Rydberg state relative to the threshold of the $O_2^+$ $c\ ^4\Sigma_u^-$ state as a function of the internuclear distance. These data are the basis of the second phase of this calculation, which is the description of the nuclear dynamics. To obtain the best ion-state potential for the nuclear dynamics, the potential energy of the $O_2^+$ $c\ ^4\Sigma_u^-$ state was computed from a multireference configuration interaction (MRCI) calculation using MOLPRO. The valence orbitals for the reference space were obtained from a state-averaged CASSCF including the lowest two $^4\Sigma_u^-$ states and the lowest two $^4\Delta_u$ states, which are the four lowest quartet $A_u$ states in the $D_{2h}$ point group used in MOLPRO. The

position of the autoionizing state relative to this ion-state potential provides the potential curve, $E_{res}(R)$, and the width $\Gamma(R)$, of the *3s* Rydberg state, which are the basis of the next step in the calculation.

We then make use of the well-established local complex potential model[66, 67] for nuclear motion on the potential surfaces of metastable electronic states that has been used extensively in such problems, including for polyatomic molecules with multiple vibrational degrees of freedom[68]. In this approach, we solve the radial Schrödinger equation for vibrational motion with a potential whose real and imaginary parts are determined by the energy and width of the metastable electronic state, in this case the *3s* Rydberg state,

$$\left[-\frac{\hbar^2}{2\mu}\frac{d^2}{dR^2} + E_{res}(R) - i\Gamma(R)/2\right]\psi_{\mathrm{v}}(R) = E_{\mathrm{v}}\psi_{\mathrm{v}}(R) \quad (3)$$

where $\mu$ is the reduced mass and $E_{res}(R)$ and $\Gamma(R)$ are the position and width of the metastable electronic state, respectively, as functions of internuclear distance.

Here the overall lifetimes of the vibrational levels, $\psi_{\mathrm{v}}(R)$, are of interest, and they arise from two effects, tunneling through the barrier indicated in Figure 1 and electronic autoionization. To calculate them directly we apply another venerable computational method, the method of exterior complex scaling (ECS)[69], to Eq. (3). The real and imaginary parts of the potential are represented with a spline interpolation and append a long range -$\alpha/R^4$ dependence to the real part beyond 5 Bohr while setting the imaginary part to zero beyond that radius. Then for values of $R > R_0$ with $R_0 = 5$ Bohr, we make the exterior complex scaling transformation on the radial coordinate of Eq. (3),

$$R \rightarrow \begin{cases} R & if\ R \le R_0 \\ R_0 + (R - R_0)e^{i\theta} & if\ R > R_0 \end{cases} \quad (4)$$

This transformation rotates the continuous part of the spectrum of eigenvalues of the Hamiltonian in Eq. (3) into the lower complex plane and exposes the complex resonance energies as discrete eigenvalues corresponding to the now square-integrable resonance wave functions, $\psi_v(R)$. The energies, $E_v$, appear as isolated complex eigenvalues.

$$E_v = E_v^{real} - i\Gamma_v/2 \quad (5)$$

The lifetime of the metastable vibrational level is given by $\tau = \hbar/\Gamma_v$. This calculation yields lifetimes that are sensitive to the details of the vibrational wave function and how it samples the *R*-dependent electronic autoionization probability described by the local complex potential, thus describing the dynamical coupling between the nuclear motion and electronic autoionization.

The ECS calculation is implemented using the grid-based discrete variable representation using methods described at length previously[70] and used many times in

ECS calculations of the complex energies of both electronic and vibrational metastable states[71-74]. In these grid-based calculations, it is a simple matter to converge the complex resonance eigenvalues so that they have no dependence on the complex scaling angle $\theta$ to many significant figures and thus represent the essentially exact solution of Eq. (3) given the local complex potential $E_{res}(R) - i\Gamma(R)/2$. The results of these calculations and their bearing on the interpretation of the lifetimes measured for the v=0 and v=1 levels of the *3s* Rydberg state will be discussed below in Sec. III C.

# III. Results

## A. Camera Image and Spatial Isolation of Wave-Mixing Emission Signals

A camera image with all three pulses temporally and spatially overlapping in the $O_2$ gas cell is shown in Figure 4(a). The light impinging on the camera is spectrally dispersed in the horizontal direction by the XUV grating, while the angular displacement in the vertical direction arises from the non-collinear wave-mixing geometry used in the experiment.

The data are presented as absorbance

$$A = -log_{10}(\frac{I}{I_0}) \qquad (6)$$

where $I$ is the intensity of light read on the CCD camera with NIR and XUV pulses, and $I_0$ is a reference signal with the XUV pulse only. Positive (red) features in the image indicate absorption while negative (blue) features indicate XUV emission in the presence of NIR pulses. There are two clear regions of signals produced at different emission angles. The region around 0 mrad, which is the direction of the XUV pulse wavevector, corresponds to transient absorption of $O_2$. It mostly mimics the depletion feature of static XUV absorption of $O_2$ at this energy region. A double-hump absorption feature is seen at the center of the peaks at 20.85 eV and 21.05 eV, representing the absorption of v=0 and v=1 levels of the *3s* Rydberg state, respectively. Complex asymmetric Fano absorption features around 23 eV arise from the v=0 and v=1 levels of the *3d* and *4s* states, and the features from 23.5 eV to 24.6 eV (the IP to the $c\ ^4\Sigma_u^-$ state) are from the absorption of *4d*, *5s*, and higher *n* Rydberg states.

Off-axis pure emission regions center around 2.4 mrad for the *3s* Rydberg state and around 1.8 mrad for higher *n* Rydberg states. These are spatially-isolated wave-mixing signals generated by one XUV photon plus two NIR photons. The angle is different for the *3s* Rydberg state and higher *n* Rydberg states due to phase matching and a slight tilt of the camera.

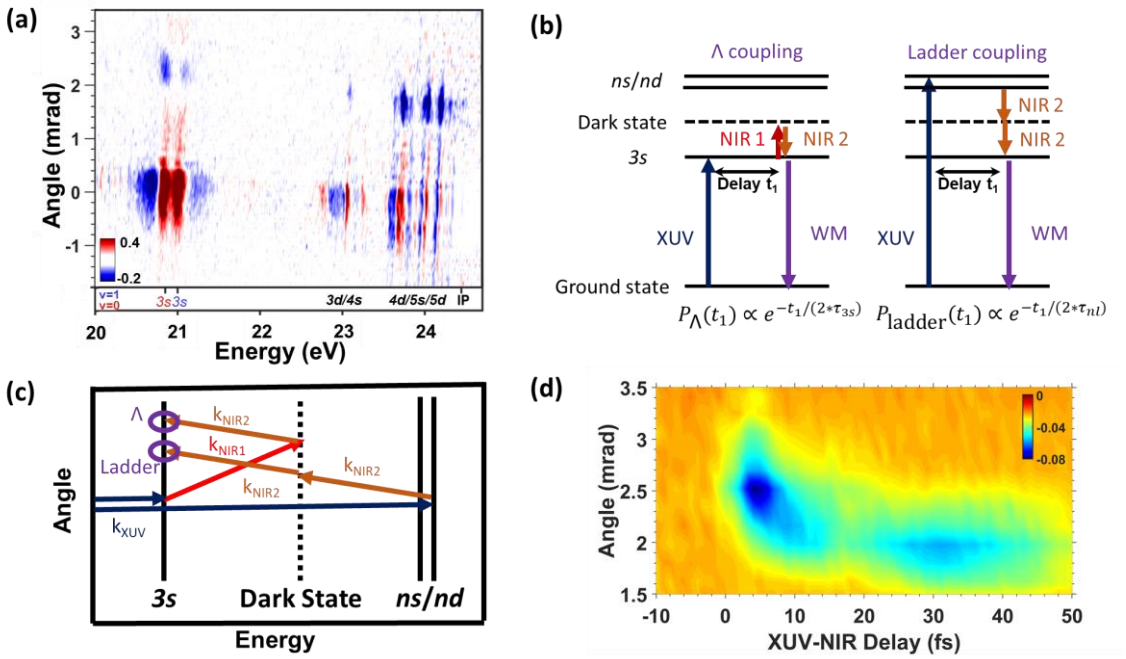


Figure 4. (a) Camera image at the overlap of all three pulses. Positive (red) features represent absorption while negative (blue) features represent emission. Spatially-isolated wave-mixing signals are observed around 1.5~2.8 mrad. (b) Two possible pathways to generate wave-mixing (WM) signals from the *3s* state. (c) Phase matching conditions and the emission angles of Λ-type coupling and ladder-type coupling (d) Angle-dependent transient wave-mixing signals of v=0 level (20.85 eV) of the *3s* Rydberg state. The component around 2.5 mrad corresponds to Λ-type coupling from *3s* Rydberg state itself while the component around 2.0 mrad corresponds to ladder-type coupling from higher *n* Rydberg states.

The wave mixing signals can be generated through the pathways shown in Figure 4(b). Briefly, an XUV photon excites the $O_2$ into its optically allowed (bright) Rydberg states. One NIR photon can couple the Rydberg states to dark states that are not accessible from the ground state, but that are allowed from the bright Rydberg states. The second NIR photon then interacts with the dark states to create a new polarization involving different or the same bright states.

There are two possible pathways to generate wave-mixing emission from the *3s* Rydberg state as shown in Figure 4(b), namely Λ-type coupling from the *3s* Rydberg state and ladder-type coupling from higher *ns*/*nd* Rydberg states. The two pathways carry different transient information reflecting the dynamics of the *3s* and the higher *ns*/*nd* states, but the emission frequencies are the same (i.e. from the *3s* state), so frequency dispersion alone is insufficient to separate the signals. To isolate the dynamics from a particular wave-mixing pathway, separation of the signals is

needed[20]. Here, we take advantage of phase matching conditions and use the emission angle of the wave-mixing signals to spatially separate these two pathways, as discussed in the next section.

### B. Angle-dependent Transient Wave-Mixing Signals and Lifetime Measurement of *3s* Rydberg state

Phase matching requires that the wavevector of the wave-mixing signal is the sum or difference of the wavevectors of XUV and NIR. The corresponding wavevector is ($k_{FWM} = k_{XUV} + k_{NIR1} - k_{NIR2}$) for Λ-type coupling and ($k_{FWM} = k_{XUV} - k_{NIR2} - k_{NIR2}$) for ladder type coupling. The emission angle of the wave-mixing signals due to the phase-matching constraint can be approximately calculated with the following expressions:

$$\varphi_{\Lambda} \approx \frac{E_{NIR1}\theta_{NIR1}+E_{NIR2}\theta_{NIR2}}{E_{WM}} \quad (7)$$

$$\varphi_{\text{ladder}} \approx \frac{2*E_{NIR2}\theta_{NIR2}}{E_{WM}} \quad (8)$$

where $\varphi_{\Lambda}$ and $\varphi_{\text{ladder}}$ are the emission angles for Λ-type and ladder-type coupling, respectively, $E_{NIR1}$ and $E_{NIR2}$ are the photon energies of the corresponding NIR pulses, $\theta_{NIR1}$ and $\theta_{NIR2}$ are the crossing angles of the corresponding NIR pulses with the XUV pulse, and $E_{WM}$ is the energy of the emitted wave-mixed photon. The photon energies of both NIR pulses are approximately 1.63 eV, as the center wavelength of the NIR pulses is around 760 nm. Since both pathways emit photons from the *3s* Rydberg states, $E_{WM}$ is 20.85 eV for the v=0 state and 21.05 eV for the v=1 state. The NIR angles are 18 mrad and 13 mrad for NIR 1 and NIR 2, respectively, as described in the experimental setup.

Using Eqs. (7) and (8), the emission angles of wave-mixing signals of v=0 level of the *3s* Rydberg state are calculated to be 2.42 mrad and 2.03 mrad for Λ-type coupling and ladder-type coupling, respectively. As shown in Figure 4(c), the two pathways should be spatially separable. To verify this, we measure the angle-dependent transient wave-mixing spectrum around 20.85 eV, the energy of the *3s* v=0 level, and the result is shown in Figure 4(d). In the transient signal, there are two distinct components at two different emission angles, one around 2.5 mrad and the other around 2 mrad. Based on the calculated emission angles, the signals around 2.5 mrad are assigned as Λ-type coupling, which carries information on the *3s* Rydberg state itself, while the component around 2 mrad is from the ladder-type coupling which carries information on higher *ns*/*nd* Rydberg states. As shown in Figure 4(d), the component around 2.5 mrad is very short-lived while the component around 2.0 mrad is longer-lived. These observations support the assignments because the higher

*ns*/*nd* states are known to be longer-lived than the *3s* state.[11, 13, 14]

We can measure lifetimes of the *3s* Rydberg state in $O_2$ by integrating the component around 2.5 mrad to get transient intensities for both v=0 and v=1 levels as shown in Figure 5. The results are then fitted with the convolution of an instrument response function with an exponential decay. Lifetimes of 5.8±0.5 fs and 4.5±0.7 fs are found for the v=0 and v=1 levels of the *3s* Rydberg state, respectively, at 95% confidence intervals. The error bars are calculated based on the fitting results on four different data sets. Based on these confidence intervals, the lifetimes of the two vibrational levels differ significantly.

The measured lifetimes reflect electronic autoionization and predissociation as shown in Eq. (1). To explain the difference in the two lifetimes, we need to ascertain the contribution of each decay channel to the overall lifetime of the two vibrational states. Invoking the ion-core approximation, one can use the predissociation lifetime for the v=0 state of the $O_2^+$ $c\ ^4\Sigma_u^-$ state, 11 ps[14], together with an electronic autoionization lifetime of 5.8 fs, to reproduce the 5.8 fs observed lifetime for that state. However, using the value of the electronic autoionization lifetime and the ion core predissociation lifetime of the v=1 state, 65 fs[13], in Eq. (2) we obtain an expected total lifetime of 5.3 fs, which is just outside the error bars for the experimental value. This suggests that nuclear motion and electronic autoionization are not completely independent. To explore this question, we performed extensive *ab initio* calculations to determine how the electronic autoionization lifetime can be affected by nuclear motion.

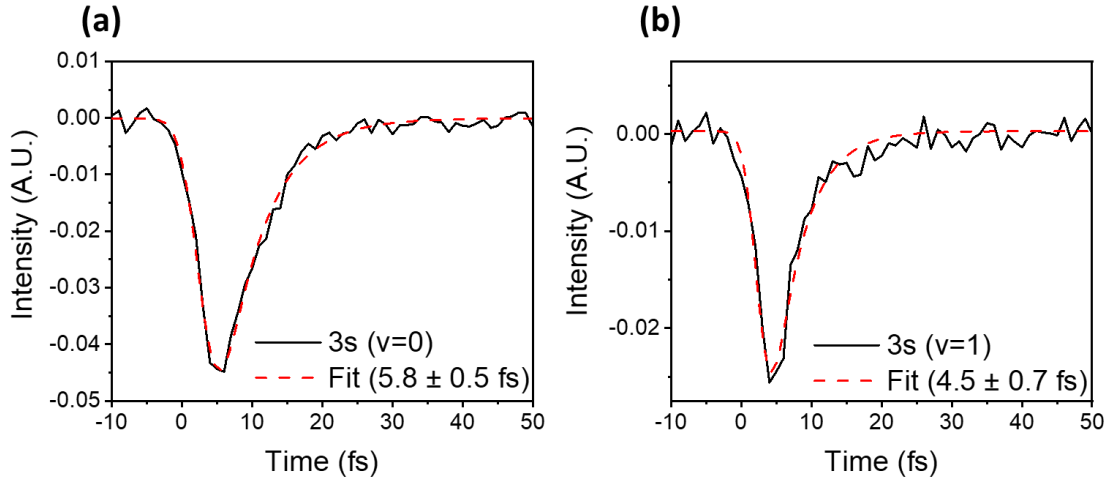


Figure 5. Transient wave-mixing signals integrated around 2.5 mrad emission angle on the camera image for the (a) v=0 (20.85 eV) and (b) v=1 levels (21.05 eV) of the *3s* Rydberg state. The black solid line is the raw data while the red dash line is the fitted curve.

### C. Coupled Vibrational and Autoionization Dynamics and Total Lifetimes of *3s* Rydberg Vibrational States

The lifetimes of the v=0 and v=1 vibrational levels of the *3s* Rydberg state arise from a competition between electronic autoionization and tunneling predissociation. It is instructive to first calculate the tunneling lifetimes of these states in the parent $c\ ^4\Sigma_u^-$ state of the cation using the MRCI potential curve shown in Figure 3 by employing the grid-based ECS numerical methods described in Sec. IIB. Tunneling lifetimes of 16.7 ps and 110 fs are obtained for the v=0 and v=1 levels, respectively. These lifetimes are notoriously difficult to calculate using *ab initio* methods, because, as explained by Tanaka and Yoshimine,[26] they depend sensitively on the details of the shallow well that arises from an avoided crossing with other $^4\Sigma_u^-$ states. By treating motion on the coupled adiabatic potentials whose avoided crossing creates the barrier shown in Figure 1, Demekhin *et al*.[36] calculated lifetimes of 12.2 ps and 67.7 fs for these two vibrational levels, in reasonable agreement with our *ab initio* values. Experimental measurements of the tunneling lifetime of the v=0 level vary from 0.27 ps[9] to 12 ps from the photoelectron spectroscopy and time-of-flight measurements of Codling *et al.*[75]. The lifetime of the v=1 level of the $O_2^+$ $c\ ^4\Sigma_u^-$ state in our calculations is in reasonably good agreement with the values of 67 and 100 fs from the measurements of Evans *et al.*[9] and Codling *et al,*[75] respectively.

The coupled vibrational and autoionization dynamics on the *3s* Rydberg state potential that lead to the observed lifetimes of the v=0 and v=1 levels of that state are summarized in Figure 6. The Fano profiles of the autoionizing feature corresponding to the *3s* state in the photoionization calculations give both the electronic autoionization width at each internuclear distance and the position of the resonance relative to its parent ionic $c\ ^4\Sigma_u^-$ state. That potential curve, shown in Figure 6(a) almost parallels the parent ion curve, but not quite, in part because the *3s* resonant state is perturbed when two ionic potential energy curves, which are the energetic thresholds for autoionization to produce those ion states, intersect it at different values of *R* in the well that binds the two vibrational levels. Those two ionic states are the $1\ ^4\Pi_g$ and $B\ ^2\Sigma_g^-$ states that are dominated by the configurations $1\sigma_g^2 1\sigma_u^2 2\sigma_g^2 2\sigma_u^2 3\sigma_g^2 1\pi_u^2 1\pi_g^3$ and $1\sigma_g^2 1\sigma_u^2 2\sigma_g^2 2\sigma_u^2 3\sigma_g^1 1\pi_u^4 1\pi_g^2$, respectively. Faint undulations and an alteration of the depth of the well change the tunneling lifetimes in the absence of autoionization. We calculate tunneling lifetimes to be 63.0 ps and 170 fs for the v=0 and v=1 levels of the *3s* Rydberg state, respectively. They are thus somewhat different from the tunneling lifetimes calculated by the same means for the parent ion state, but the differences are not surprising if we keep in mind the semiclassical picture that tunneling probabilities depend exponentially on small changes in the potential.[76]

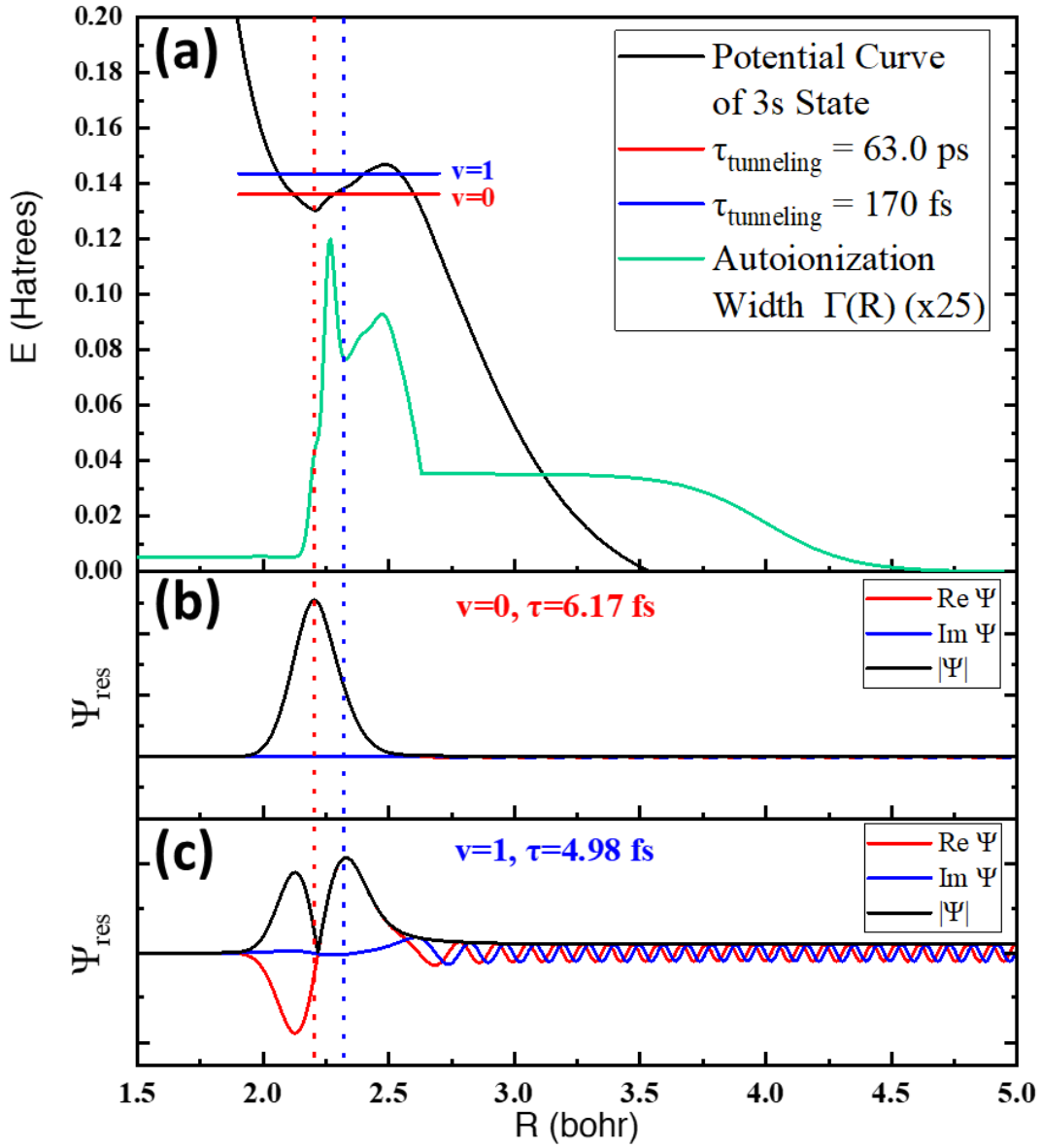


Figure 6. Vibrational dynamics on the calculated *3s* Rydberg potential curve whose imaginary part is given by the *R*-dependent electronic autoionization width in the local complex potential, $E_{res}(R) - i\Gamma(R)/2$. (a) Potential curve $E_{res}(R)$, width $\Gamma(R)$ , and location of tunneling vibrational levels, (b) the v=0 vibrational wave function, and (c) the v=1 vibrational wave function showing tunneling into the dissociative region of the potential. Red and blue vertical dash lines mark the location of the maxima in the absolute value of the vibrational wave functions of v=0 and v=1, respectively.

More striking in both Figures 3 and 6 is the strong structure in the width of the *3s* Rydberg Fano resonance feature as a function of internuclear distance. As each of the

two thresholds (the $1\ ^4\Pi_g$ and $B\ ^2\Sigma_g^-$ states of $O_2^+$) shown in Figure 3 pass through the *3s* state with increasing internuclear distance, an autoionization decay channel opens, and the competition between the changing decay pathways alters the total ionization width. How the variation in the total electronic autoionization width affects the vibrational states depends on the structure of the vibrational wave functions in this critical region. Those wave functions are also shown in Figure 6, and their extension to large R outside the tunneling barrier is an indication of the tunneling probability. The fits to the calculated width shown in Figures 3 and 6 are extended outside the well, but none of the calculated results depend (to five significant figures) on the width outside the well. Inside the well the story is very different.

## IV. Discussion

The initial calculation of the lifetimes of the states using this local complex potential gave lifetimes of 4.67 and 4.93 fs for the v=0 and v=1 levels of the *3s* Rydberg state, respectively, retaining several significant figures, giving the opposite trend from the experimental values of 5.8 and 4.5 fs. However, the calculated lifetimes are dramatically sensitive to the details of the electronic autoionization width appearing in Eq. (3) as the imaginary part of the local complex potential. Shifting the width curve to larger values of R by only 0.03 Bohr (hardly the width of the line in Figure 6) produces lifetimes of 6.17 fs and 4.98 fs for the v=0 and v=1 levels, thereby reproducing the experimental trend of a shorter v=1 lifetime. Moreover, both values lie within the error bars of the experimental lifetimes.

The reason for this sensitivity to the variation of the electronic autoionization lifetime with internuclear distance is apparent in Figure 6. The wave functions of the two metastable vibrational states sample the variations in the autoionization probability quite differently. If we perform the computational experiment of shifting the calculated width function slightly to the right (to larger R by a few hundredths of a Bohr), the lifetime of the v=0 state increases quickly as the peak in $\Gamma(R)$ begins to move out of the range of R where the v=0 wave function is nonzero. The v=1 wave function extends over a larger range of R and its lifetime changes little for small shifts, but for larger shifts its lifetime increases more quickly. This computational test shows that the observed lifetime is extremely sensitive to the dependence of the autoionization probability on internuclear distance. This degree of sensitivity of the lifetimes of these metastable states makes their experimental observation a powerful test of all parts of their theoretical description.

It is important to note that neither of these two calculations can be reproduced with Eq. (2) using the calculated tunneling lifetimes $\tau_d^{(\mathrm{v=0})}$= 63.0 ps and $\tau_d^{(\mathrm{v=1})}$= 170 fs for these states with any single value of the electronic autoionizing width $\tau_a^{(3s)}$,

which suggests the simple picture of the assumption that the autoionization lifetime is independent of vibrational levels described by Eq. (2) has broken down here. We can substitute the calculated overall and tunneling lifetimes into Eq. (1) to find the autoionization lifetime at different vibrational levels as shown in Table 1. The autoionization lifetime decreases by about 20% from v=0 to v=1, which dominates most of the change in total lifetime.

These calculations are not of spectroscopic accuracy, of course, and we are unaware of any calculations of such accuracy for this difficult problem, either for the $O_2^+$ $c\ ^4\Sigma_u^-$ state or the Rydberg states converging to it. However, they do strongly suggest that the measurement of these lifetimes probes the dynamical coupling between internuclear separation and electronic autoionization, while the tunneling contribution to predissociation is a weak spectator to lifetime process. The combination of *ab initio* electronic structure and photoionization calculations and the experimental observations provide strong evidence that the electronic autoionization lifetime can change significantly with internuclear distance and thus different vibrational levels can have different autoionization lifetimes.

| | Experimental | Theoretical | | |
|---|---|---|---|---|
| | Lifetime | Lifetime | Autoionization | Predissociation |
| v=0 | 5.8±0.5 fs | 6.17 fs | 6.17 fs | 63 ps |
| v=1 | 4.5±0.7 fs | 4.98 fs | 5.13 fs | 170 fs |
| Difference | 28.8±17.2 % | 23.9% | 20.0% | >100% |

Table 1. Experimental and theoretical results on the lifetime of *3s* Rydberg state.

## V. Conclusions

We performed attosecond XUV wave-mixing spectroscopy on the short-lived *3s* Rydberg state, part of a series that converges to the $O_2^+$ $c\ ^4\Sigma_u^-$ state. The lifetimes of the v=0 and v=1 vibrational levels of the *3s* Rydberg state are measured to be 5.8±0.5 fs and 4.5±0.7 fs, respectively. Our time-domain measurements find that the lifetime of two different vibrational levels of the *3s* Rydberg state are significantly different from each other, and this difference cannot be explained by the change of the predissociation rate alone as proposed previously.[11, 37] Instead, with the aid of the theoretical results described here, we find that more rapid electronic autoionization in the v=1 state contributes significantly to the decreased lifetime of this state. This effect is dramatically sensitive to the details of the dependence of the autoionization width on internuclear distance. The excellent agreement between experimental and calculated lifetimes provides strong evidence for this key theoretical result.

The work described herein is the first experiment performed with attosecond XUV wave-mixing spectroscopy to investigate the ultrafast decaying states in a molecule. We demonstrate the ability of attosecond XUV wave-mixing spectroscopy to probe dynamics on the few-fs timescale as well as the ability to probe the vibrationally resolved lifetimes in a molecule. Our theoretical calculations shed light on the interplay between the vibrational motion, tunneling, and the autoionization process which is strongly influenced by crossings with ionic states. This detailed understanding will lead to many possible applications of attosecond XUV wave-mixing spectroscopy in the future.

## Conflicts of interest

There are no conflicts of interest to declare.

## Acknowledgments

Work at LBNL was performed under the auspices of the US DOE under Contract DE-AC02-05CH11231, the Atomic, Molecular and Optical Sciences Program, supported by the U.S. DOE Office of Basic Energy Sciences, Division of Chemical Sciences. A.S. received support from the U.S. Department of Energy (DOE), Office of Science, Basic Energy Sciences (BES) under Award No. DE-SC0018251. A.P.F. acknowledges funding from the National Science Foundation Graduate Research Fellowship Program.

## References

1 R. Stephen Berry and Svend Erik Nielsen, *Phy. Rev. A*, 1970, **1**, 395-411.

2 A. Giusti-Suzor and C. Jungen, *J. Chem. Phy.*, 1984, **80**, 986-1000.

3 H. Lefebvre-Brion and F. Keller, *J. Chem. Phy.*, 1989, **90**, 7176-7183.

4 F. Texier, C. Jungen and S. C. Ross, *Faraday Discuss.*, 2000, **115**, 71-78.

5 Y. Hikosaka, P. Lablanquie, M. Ahmad, R. I. Hall, J. G. Lambourne, F. Penent and J. H. D. Eland, *J. Phys. B: At. Mol. Opt. Phys.*, 2003, **36**, 4311.

6 H. Lefebvre-Brion and R. W. Field, *The Spectra and Dynamics of Diatomic Molecules* , 2004.

7 A. N. Heays, A. D. Bosman and E. F. v. Dishoeck, *Astron. Astrophys.*, 2017, **602**, A105.

8 T. Akahori, Y. Morioka, M. Watanabe, T. Hayaishi, K. Ito and M. Nakamura, *J. Phys. B: At. Mol. Opt. Phys.*, 1985, **18**, 2219-2229.

9 M. Evans, S. Stimson, C. Y. Ng and C. -. Hsu, *J. Chem. Phy.*, 1998, **109**, 1285-1292.

10 H. Liebel, A. Ehresmann, H. Schmoranzer, P. V. Demekhin, B. M. Lagutin and V. L. Sukhorukov, *J. Phys. B: At. Mol. Opt. Phys.*, 2002, **35**, 895-905.

11 A. Ehresmann, L. Werner, S. Klumpp, H. Schmoranzer, P. V. Demekhin, B. M. Lagutin, V. L. Sukhorukov, S. Mickat, S. Kammer, B. Zimmermann and K. Schartner, *J. Phys. B: At. Mol. Opt. Phys.*, 2004, **37**, 4405-4422.

12 L. Fan, Z. Zhong, L. Zhu, X. Liu, Z. Yuan, J. Sun and K. Xu, *Phy. Rev. A*, 2005, **71**, 032704.

13 B. Doughty, C. J. Koh, L. H. Haber and S. R. Leone, *J. Chem. Phy.*, 2012, **136**, 214303.

14 H. Timmers, N. Shivaram and A. Sandhu, *Phy. Rev. Lett.*, 2012, **109**, 173001.

15 C. Liao, X. Li, D. J. Haxton, T. N. Rescigno, R. R. Lucchese, C. W. McCurdy and A. Sandhu, *Phy. Rev. A*, 2017, **95**, 043427.

16 A. Plunkett, N. Harkema, R. R. Lucchese, C. W. McCurdy and A. Sandhu, *Phy. Rev. A*, 2019, **99**, 063403.

17 W. Cao, E. R. Warrick, A. Fidler, D. M. Neumark and S. R. Leone, *Phy. Rev. A*, 2016, **94**, 053846.

18 W. Cao, E. R. Warrick, A. Fidler, S. R. Leone and D. M. Neumark, *Phy. Rev. A*, 2018, **97**, 023401.

19 E. R. Warrick, A. P. Fidler, W. Cao, E. Bloch, D. M. Neumark and S. R. Leone, *Faraday Discuss.*, 2018, **212**, 157-174.

20 H. J. B. Marroux, A. P. Fidler, D. M. Neumark and S. R. Leone, *Sci. Adv.*, 2018, **4**, eaau3783.

21 A. P. Fidler, H. J. B. Marroux, E. R. Warrick, E. Bloch, W. Cao, S. R. Leone and D. M. Neumark, *J. Chem. Phy.*, 2019, **151**, 114305.

22 A. P. Fidler, S. J. Camp, E. R. Warrick, E. Bloch, H. J. B. Marroux, D. M. Neumark, K. J. Schafer, M. B. Gaarde and S. R. Leone, *Nat. Commun.*, 2019, **10**, 1384.

23 A. P. Fidler, E. R. Warrick, H. J. B. Marroux, E. Bloch, D. M. Neumark and S. R. Leone, *J. Phy.: Photonics*, 2020, **2**, 34003.

24 K. Codling and R. P. Madden, *J. Chem. Phy.*, 1965, **42**, 3935-3938.

25 O. Edqvist, E. Lindholm, L. E. Selin and L. Åsbrink, *Phys. Scr.*, 1970, **1**, 25-30.

26 K. Tanakaa and M. Yoshimine, *J. Chem. Phy.*, 1979, **70**, 1626-1633.

27 M. A. Dillon and D. Spence, *J. Chem. Phy.*, 1981, **74**, 6070-6074.

28 L. J. Frasinski, K. J. Randall and K. Codling, *J. Phys. B: At. Mol. Opt. Phys.*, 1985, **18**, L129-L135.

29 M. Richard-Viard, O. Dutuit, M. Ait-Kaci and P. M. Guyon, *J. Phys. B: At. Mol. Opt. Phys.*, 1987, **20**, 2247-2254.

30 J. W. Gallagher, C. E. Brion, J. A. R. Samson and P. W. Langhoff, *J. Phys. Chem. Ref. Data*, 1988, **17**, 9-153.

31 B. WannBerg, L.Karisson and M. Carlsson Gothe, *Phy. Rev. A*, 1992, **45**, 4374-4383.

32 D. M. P. Holland, D. A. Shaw, S. M. McSweeney, M. A. MacDonald, A. Hopkirk and M. A. Hayes, *Chem. Phy.*, 1993, **173**, 315-331.

33 K. Ellis, R. I. Hall, L. Avaldi, G. Dawber, A. McConkey, L. Andric and G. C. King, *J. Phys. B: At. Mol. Opt. Phys.*, 1994, **27**, 3415-3426.

34 H. Liebel, S. Lauer, F. Vollweiler, R. Müller-Albrecht, A. Ehresmann, H. Schmoranzer, G. Mentzel, K. -. Schartner and O. Wilhelmi, *Phy. Lett. A*, 2000, **267**, 357-369.

35 A. Karawajczyk, P. Erman, E. Rachlew-Källne, J. R. i. Riu, M. Stankiewicz, K. Y. Franzén and L. Veseth, *Phy. Rev. A*, 2000, **61**, 032718.

36 F. V. Demekhin, D. V. Omel'yanenko, B. M. Lagutin, V. L. Sukhorukov, L. Werner, A. Ehresmann, K. -. Schartner and H. Schmoranzer, *Russ. J. Phys. Chem. B*, 2007, **1**, 213-221.

37 P. V. Demekhin, D. V. Omel'yanenko, B. M. Lagutin, V. L. Sukhorukov, L. Werner, A. Ehresmann, K. -. Schartner and H. Schmoranzer, *Opt. Spectrosc*, 2007, **102**, 318-329.

38 A. Padmanabhan, M. A. MacDonald, C. H. Ryan, L. Zuin and T. J. Reddish, *J. Phys. B: At. Mol. Opt. Phys.*, 2010, **43**, 165204.

39 P. Peng, C. Marceau, M. Hervé, P. B. Corkum, A. Y. Naumov and D. M. Villeneuve, *Nat. Commun.*, 2019, **10**, 5269-8.

40 J. R. Taylor, *Scattering theory: The quantum theory of nonrelativistic collisions*, Dover Publications, Inc, Mineola, New York, 2012.

41 M. Ukai, S. Machida, K. Kameta, N. Kouchi, Y. Hatano and K. ito, *Phy. Rev. Lett.*, 1995, **74**, 239-242.

42 M. N. Piancastelli, R. F. Fink, R. Feifel, M. Bässler, S. L. Sorensen, C. Miron, H. Wang, I. Hjelte, O. Björneholm, A. Ausmees, S. Svensson, P. Salek, F. K. Gel'mukhanov and H. Ågren, *J. Phys. B: At. Mol. Opt. Phys.*, 2000, **33**, 1819-1826.

43 Q. Bian, Y. Wu, J. G. Wang and S. B. Zhang, *Phy. Rev. A*, 2019, **99**, 033404.

44 H. J. B. Marroux, A. P. Fidler, A. Ghosh, Y. Kobayashi, K. Gokhberg, A. I. Kuleff, S. R. Leone and D. M. Neumark, *Nat. Commun.*, (accepeted), .

45 P. M..Paul, E.S.Toma, P.Breger, G.Mullot, F. Auge, Ph.Balcou, H.G.Muller and P.Agostini, *Science*, 2001, **292**, 1689-1692.

46 M. Chini, K. Zhao and Z. Chang, *Nat. Photonics*, 2014, **8**, 178-186.

47 A. Rundquist, *Science*, 1998, **280**, 1412-1415.

48 H. Wang, M. Chini, S. Chen, C. Zhang, F. He, Y. Cheng, Y. Wu, U. Thumm and Z. Chang, *Phy. Rev. Lett.*, 2010, **105**, 143002.

49 M. Chini, B. Zhao, H. Wang, Y. Cheng, S. X. Hu and Z. Chang, *Phy. Rev. Lett.*, 2012, **109**, 073601.

50 C. Ott, A. Kaldun, P. Raith, K. Meyer, M. Laux, J. Evers, C. H. Keitel, C. H. Greene and T. Pfeifer, *Science*, 2013, **340**, 716-720.

51 A. R. Beck, B. Bernhardt, E. R. Warrick, M. Wu, S. Chen, M. B. Gaarde, K. J. Schafer, D. M. Neumark and S. R. Leone, *New J. Phys.*, 2014, **16**, 113016.

52 X. Li, B. Bernhardt, A. R. Beck, E. R. Warrick, A. N. Pfeiffer, M. Justine Bell, D. J. Haxton, C. William McCurdy, D. M. Neumark and S. R. Leone, *J. Phys. B: At. Mol. Opt. Phys.*, 2015, **48**, 125601.

53 E. R. Warrick, W. Cao, D. M. Neumark and S. R. Leone, *J. Phy. Chem. A*, 2016, **120**, 3165-3174.

54 E. R. Warrick, J. E. Bækhøj, W. Cao, A. P. Fidler, F. Jensen, L. B. Madsen, S. R. Leone and D. M. Neumark, *Chem. Phy. Lett.*, 2017, **683**, 408-415.

55 Y. Kobayashi, K. F. Chang, T. Zeng, D. M. Neumark and S. R. Leone, *Science*, 2019, **365**, 79-83.

56 H. Timmers, Y. Kobayashi, K. F. Chang, M. Reduzzi, D. M. Neumark and S. R. Leone, *Opt. Lett.*, 2017, **42**, 811-814.

57 R. E. Stratmann and R. R. Lucchese, *J. Chem. Phy.*, 1995, **102**, 8493-8505.

58 R. E. Stratmann, Robert W. Zurales and Robert R. Lucchese, *J. Chem. Phy.*, 1996, **104**, 8989-9000.

59 R. R. Lucchese, *J. Chem. Phy.*, 1990, **92**, 4203-4211.

60 A. Lafosse, J. C. Brenot, P. M. Guyon, J. C. Houver, A. V. Golovin, M. Lebech, D. Dowek, P. Lin and R. R. Lucchese, *J. Chem. Phy.*, 2002, **117**, 8368-8384.

61 P. Lin and R. R. Lucchese, *J. Chem. Phy.*, 2002, **116**, 8863-8875.

62 T. H. Dunning, *J. Chem. Phy.*, 1989, **90**, 1007-1023.

63 R. A. Kendall, T. H. Dunning and R. J. Harrison, *J. Chem. Phy.*, 1992, **96**, 6796-6806.

64 H. Werner, P. J. Knowles, G. Knizia, F. R. Manby and M. Schütz, *Wiley Interdiscip. Rev. Comput. Mol. Sci.*, 2012, **2**, 242-253.

65 H.-J. Werner, P. J. Knowles, G. Knizia, F. R. Manby, M. Schütz, P. Celani, T. Korona, R. Lindh, A. Mitrushenkov, G. Rauhut, K. R. Shamasundar, T. B. Adler, R. D. Amos, A. Bernhardsson, A. Berning, D. L. Cooper, M. J. O. Deegan, A. J. Dobbyn, F. Eckert, E. Goll, C. Hampel, A. Hesselmann, G. Hetzer, T. Hrenar, G. Jansen, C. Köppl, Y. Liu, A. W. Lloyd, R. A. Mata, A. J. May, S. J. McNicholas, W. Meyer, M. E. Mura, A. Nicklass, D. P. O'Neill, P. Palmieri, D. Peng, K. Pflüger, R. Pitzer, M. Reiher, T. Shiozaki, H. Stoll, A. J. Stone, R. Tarroni, T. Thorsteinsson and M.Wang, *http://www.molpro.net*, 2015, .

66 T. F. O'Malley, *Phy. Rev.*, 1966, **150**, 14-29.

67 L. Dube and A. Herzenberg, *Phys. Rev. A*, 1979, **20**, 197-213.

68 D. Haxton, T. Rescigno and C. McCurdy, *Phy. Rev. A*, 2007, **75**, 012711.

69 B. Simon, *Phy. Rev. A*, 1979, **71**, 211-214.

70 C. W. McCurdy, M. Baertschy and T. N. Rescigno, *J. Phys. B: At. Mol. Opt. Phys.*, 2004, **37**, R137-R187.

71 C. W. McCurdy and F. Martín, *J. Phys. B: At. Mol. Opt. Phys.*, 2004, **37**, 917-936.

72 W. Vanroose, D. A. Horner, F. Martin, T. N. Rescigno and C. W. McCurdy, *Phy. Rev. A*, 2006, **74**, 052702.

73 A. Scrinzi, *Phy. Rev. A*, 2010, **81**, 053845.

74 D. Hvizdoš, M. Váňa, K. Houfek, C. H. Greene, T. N. Rescigno, C. W. McCurdy and R. Čurík, *Phy. Rev. A*, 2018, **97**, 022704.

75 K. Codling, L. J. Frasinski and K. J. Randall, *J. Phys. B: At. Mol. Opt. Phys.*, 1985, **18**, L251-L257.

76 E. Merzbacher, *Quantum mechanics*, J. Wiley, 1970.